Fuel 290 (2021) 119887

Contents lists available at ScienceDirect

Fuel

journal homepage: www.elsevier.com/locate/fuel

Full Length Article

Effects of ambient pressure and nozzle diameter on ignition characteristics in diesel spray combustion

Jiun Cai Ong [a,*], Jens Honore Walther [a,b], Shijie Xu [c], Shenghui Zhong [c,d], Xue-Song Bai [c], Kar Mun Pang [e]

[a] Department of Mechanical Engineering, Technical University of Denmark, Nils Koppels Allé, 2800 Kgs Lyngby, Denmark
[b] Computational Science and Engineering Laboratory, ETH Zürich, Clausiusstrasse 33, Zürich CH-8092, Switzerland
[c] Department of Energy Sciences, Lund University, 22100 Lund, Sweden
[d] State Key Laboratory of Engines, Tianjin University, 135 Yaguan Rd, Tianjin 300350, China
[e] MAN Energy Solutions, Teglholmsgade 41, 2450 København SV, Denmark

ARTICLE INFO

Keywords:
Spray flame
Transported probability density function
Ignition process
Ambient density effect
Nozzle diameter effect

ABSTRACT

Numerical simulations are performed to investigate the effects of ambient density (ρ_{am}) and nozzle diameter (D_{noz}) on the ignition characteristic of diesel spray combustion under engine-like conditions. A total of nine cases which consist of different ρ_{am} of 14.8, 30.0, and 58.5 kg/m^3 and different D_{noz} of 100, 180, and 363 μm are considered. The results show that the predicted ignition delay times are in good agreement with measurements. The current results show that the mixture at the spray central region becomes more fuel-rich as D_{noz} increases. This leads to a shift in the high-temperature ignition location from the spray tip towards the spray periphery as D_{noz} increases at ρ_{am} of 14.8 kg/m^3. At higher ρ_{am} of 30.0 and 58.5 kg/m^3, the ignition locations for all D_{noz} cases occur at the spray periphery due to shorter ignition timing and the overly fuel-rich spray central region. The numerical results show that the first ignition location during the high-temperature ignition occurs at the fuel-rich region at $\rho_{am} \leqslant 30.0$ kg/m^3 across different D_{noz}. At $\rho_{am} = 58.5$ kg/m^3, the ignition occurs at the fuel-lean region for the 100 and 180 μm cases, but at the fuel-rich region for the 363 μm nozzle case. This distinctive difference in the result at 58.5 kg/m^3 is likely due to the relatively longer ignition delay time in the 363 μm nozzle case. Furthermore, the longer ignition delay time as D_{noz} increases can be related to the higher local scalar dissipation rate in the large nozzle case.

1. Introduction

Automotive and marine industries have worked to improve the understanding of in-cylinder processes in order to design engines that are cleaner and more efficient. Sandia National Laboratory and numerous research groups have shared their optical measurements and numerical modeling results through the Engine Combustion Network (ECN) [1] to facilitate the study of diesel spray combustion and for validation of numerical model. Effects of a wide range of diesel engine parameters on fuel penetration, ignition delay time (IDT), flame lift-off length (LOL), and soot emissions have been studied [2–4]. Extensive and comprehensive studies have been carried out for Spray A configuration, where the ambient gas density (ρ_{am}) and nozzle diameter size (D_{noz}) are set to 22.8 kg/m^3 and 90 μm, respectively. The ambient temperature (T_{am}) is set to 900 K, while its corresponding ambient pressure (P_{am}) is 58 bar. Significant emphasis has been placed on understanding its ignition and flame stabilization processes [5–8]. It was only recently that ECN introduced the Spray D configuration [9,10], which has the same operating conditions as Spray A, but uses a larger nozzle diameter, $D_{noz} = 186$ μm. Different ignition characteristics were observed in Spray D than that in Spray A at 900 K, where ignition was shown to occur at the spray periphery in the former case [10] instead of occurring at the spray head for the latter case. The results suggest that the favorable ignition location shifts to the peripheral of the spray as nozzle diameter increases.

It is important to note that most of the aforementioned studies were performed at ambient density, $\rho_{am} = 14.8$–30.0 kg/m^3. However, the ρ_{am} at the start of injection is approximately 60.0 kg/m^3 under full load conditions in typical heavy-duty engines and large two-stroke marine engines. Meanwhile, the D_{noz} in marine engines is generally larger in

* Corresponding author.
E-mail address: jcong@mek.dtu.dk (J.C. Ong).

https://doi.org/10.1016/j.fuel.2020.119887
Received 16 September 2020; Received in revised form 13 November 2020; Accepted 26 November 2020
Available online 2 January 2021

order to deliver a greater amount of fuel. For instance, the fuel injector in the medium-speed four-stroke marine engines simulated by Kyriakides et al. [11] and Kilpinen [12] had a size of 370 μm and 388 μm, respectively. Ishibashi and Tsuru [13] performed multiple injection experiments under marine engine-like conditions, in which the pilot diesel injector and main diesel injector had a size of 160 μm and 500 μm, respectively. Schmid et al. [14] conducted experiments using an optical accessible marine spray combustion chamber with swirling flow, in which the fuel is injected from a 875 μm nozzle. Bolla et al. [15] later used the same experimental setup to study a range of D_{noz} from 200 to 1200 μm. However, it is important to note that the experiment is only conducted at a constant density of 33 kg/m^3. Experimental studies of spray combustion conducted in a constant volume chamber under high ρ_{am} (or P_{am}) and large D_{noz} were reported by Siebers and co-workers [3,16–19]. The experimental studies were carried out for a range of ρ_{am} from 7.3 to 58.5 kg/m^3, which corresponds to P_{am} of 20 to 170 bar when T_{am} is at 1000 K. Both liquid and vapor penetration lengths were found to decrease with increasing ρ_{am}. Meanwhile, spray flame at quasi-steady state were found to reduce in size (both in length and width) when ρ_{am} increases [3,18]. In terms of ignition and premixed combustion processes, Higgins et al. [19] investigated them up to 45.0 kg/m^3 but only for D_{noz} of 246 μm. Their work showed that increasing density decreases the time for ignition to occur. In addition, the ignition location was shown to move around the central region of the spray containing liquid-phase fuel and extend upstream along its sides.

From a simulation point of view, Cung et al. [20] performed Unsteady Reynolds Averaged Navier-Stokes (URANS) simulations to study the influence of D_{noz} on spray combustion and soot emissions under Spray A conditions. The SAGE detailed chemistry solver [21], which is a well-mixed reactor based model, was used in the study. The tested D_{noz} ranged from 30 to 129 μm. They noticed that the IDT varies non-linearly with D_{noz} where the shortest ignition delay occurs for the 70 μm nozzle case. Nozzles with smaller diameter delayed the ignition due to leaner mixture (less injected fuel mass and high levels of air entrainment) at ignition sites [20]. As the nozzle diameter decreased, the equivalence ratio contour line shifted toward leaner mixtures at the same axis location. Comparison of Spray A and Spray D was carried out in the numerical study by Desantes et al. [22]. The unsteady flamelet progress variable (UFPV) model was employed in the study. It was shown that a reduction in D_{noz} promotes faster mixing which shortens the time needed to reach ignitable equivalence ratio, therefore a shorter IDT was observed in the Spray A case. In addition, Ong et al. [23] compared the ignition characteristics between Spray A and Spray D by performing large eddy simulations coupled with partially-stirred reactor model. Their simulations were able to predict the annular ignition sites for Spray D at ambient temperatures of 1000 and 900 K, which is consistent with the experimental observation in [10]. It was suggested by Ong et al. [23] that the less fuel-rich mixture at the spray periphery is more favorable for ignition than the relatively more fuel-rich mixture at the core of the spray in Spray D. Pang et al. [24] performed a URANS study on reacting sprays in a constant volume combustion vessel with D_{noz} of 100, 180, and 363 μm. Their numerical results showed that as D_{noz} becomes larger, the low-temperature region of the spray tends to get more fuel-rich. Their simulation was able to capture the spray flame feature across different D_{noz}, in particular the flame penetration length. However, little focus was placed on the ignition characteristic of different D_{noz}.

All the numerical works mentioned above for different D_{noz} were only performed at a single ρ_{am}. On the other hand, the effects of ρ_{am} on ignition and spray flame were carried out by Pang et al. [25]. Their 3-D numerical study investigated the ignition behaviors and flame structures at different ρ_{am} of 14.8, 30.0, and 58.5 kg/m^3. They found that the mixture fraction (Z) of the first igniting location during the high-temperature ignition does not vary monotonically with ρ_{am}. The ignition occurred at a fuel-rich mixture region for the 14.8 and 30.0 kg/m^3 cases, but at a fuel-lean mixture region for the 58.5 kg/m^3 case. It is important to note that the work was carried out only for a single D_{noz} of 180 μm. The coupled effects between D_{noz} and ρ_{am} on ignition characteristics are still not completely understood. The variation of the ignition mixture during initial high-temperature ignition with respect to ρ_{am} may vary as D_{noz} becomes larger or smaller. This information is critical to the development of skeletal surrogate fuel mechanisms. Developing a mechanism that fits into a narrower range of operating conditions would allow the size of the fuel mechanisms to be further optimized, thus increasing computational efficiency.

Set against these backgrounds, the objective of the present numerical work is to investigate the effects of varying D_{noz} and ρ_{am} on the ignition process in diesel spray flame. The velocity, species, and temperature distribution profiles are computed and compared to elucidate the differences in the ignition process. The paper is structured such that experimental data used for model validation are first described in Section 2. Next is the descriptions of the numerical methods in Section 3. Sections 4 and 5 present the model validation as well as the numerical analysis of the autoignition process at different ρ_{am} and D_{noz}. Conclusions from this work are highlighted in the final section.

Table A1
Operating conditions and injection specifications.

Case	O_2 [% mol]	T_{am} [K]	ρ_{am} [kg/m^3]	D_{noz} [μm]	P_{inj} [bar]	$\dot{m}_f$ [g/s]
1	21	1000	14.8	100	1400	2.7
2	21	1000	30.0	100	1400	2.8
3*	21	1000	58.5	100	1400	2.8
4	21	1000	14.8	180	1400	8.8
5	21	1000	30.0	180	1400	9.0
6	21	1000	58.5	180	1400	9.2
7	21	1000	14.8	363	1400	35.8
8	21	1000	30.0	363	1400	36.3
9*	21	1000	58.5	363	1400	36.3

* No experimental injected fuel mass flow rate ($\dot{m}_f$) is available for ρ_{am} = 58.5 kg/m^3. The $\dot{m}_f$ for ρ_{am} = 30.0 kg/m^3 case is used instead.

2. Case descriptions

The grade number two Diesel fuel (Diesel #2) spray experimental data [1,17,18] obtained from constant volume spray combustion experiment is used for model validation in this work. The constant volume chamber has an ambient gas composition of 21.0% O_2, 69.3% N_2, 6.1% CO_2 and 3.6% H_2O (by volume) before the start of spray injection. This experimental ambient gas composition is used in the current reacting spray cases to ensure identical initial thermochemical conditions.

As depicted in Table A1, reacting spray simulations are carried out for three D_{noz} of 100, 180, and 363 μm. Three ρ_{am} of 14.8, 30.0, and 58.5 kg/m^3 are considered for each D_{noz}. At T_{am} = 1000 K, the ρ_{am} considered corresponds to P_{am} of 42, 85, and 170 bar, respectively. Initial flow and turbulence conditions can be found in the previous work [26]. The operating conditions and the injection specifications, such as D_{noz}, injection pressure (P_{inj}), and injected fuel mass flow rate ($\dot{m}_f$), for each test cases are listed in Table A1.

3. CFD model formulation

The 3-D CFD spray combustion simulations are carried out using OpenFOAM-v1712. The fuel spray, flow, and combustion processes are modeled using the Eulerian-Lagrangian approach within the URANS framework. The realizable k-ϵ model [27] is employed for turbulence modeling. The injected liquid phase of the fuel is modeled as discrete parcels whose motion is described using the Lagrangian particle tracking approach. Each parcel represents a group of spherical droplets whose position, size, and physical properties are similar. Primary breakup of the injected fuel is considered by injecting computational parcels with

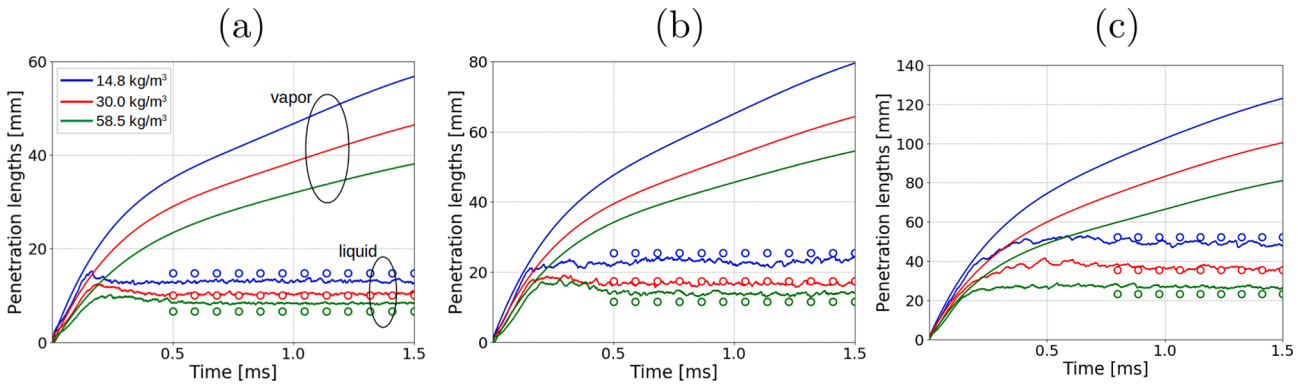

Fig. 1. Liquid and vapor penetration lengths of the non-reacting sprays as a function of time after start of injection (ASI) for different D_{noz} of (a) 100, (b) 180, and (c) 363 μm. Solid lines denote the simulations results. Circle markers denote the liquid scaling law results [16].

the Rosin-Rammler distribution of diameter ranging from $0.1D_{noz}$ to D_{noz}. The reference diameter, D_{ref} and exponent for the Rosin-Rammler disribution are set to $0.7D_{noz}$ and 3.0, respectively. The secondary breakup is modeled by the Reitz-Diwakar spray model [28]. As each nozzle has its own nozzle coefficients (available in [1]), the stripping breakup constant, C_s, in the Reitz-Diwakar model for the nozzle cases of 100, 180, and 363 μm are set to 13, 6, and 8, respectively. It is important to note that for each D_{noz} case the same C_s value is used across the three ρ_{am} tested. The liquid properties of tetradecane ($C_{14}H_{30}$) are used to represent Diesel #2 fuel [29]. The Frossling model and the Ranz-Marshall correlation are employed to account for the droplet evaporation and heat transfer with the surrounding gas phase respectively.

The turbulence-chemistry interaction (TCI) is modeled using an Eulerian-based transported probability density function (PDF) method, the Eulerian Stochastic Field (ESF) method [30]. Similar to the Lagrangian particle transported PDF method, the ESF method is a general approach to account for TCI effect. It can be used to simulate the autoignition as well as different levels of "premixedness", *i.e.*, premixed, partially premixed, and non-premixed. Details of the ESF formulation are available in [30]. The model has been applied successfully to simulate diesel spray combustion [24,25,31,32]. The number of stochastic fields is set to 32 as the result was shown to have reached convergence [32]. The Chemistry Coordinate Mapping (CCM) approach is coupled with the ESF solver to speed up the integration process of the chemical reaction rates [33]. The current work uses a four-dimensional phase space based on temperature, local equivalence ratio, scalar dissipation rate, and the mass fraction of fuel, where the resolutions of CCM are fixed at 5 K, 0.01, 0.025, and 0.001, respectively [32,33].

The computational domain is a constant volume cubic chamber with side lengths of 108 mm, which corresponds to the volume of the experimental combustion vessel [1]. The ambient mixture composition, pressure, and temperature are initiated as uniform field while the velocity field is set to zero. All boundaries are set as no-slip wall with Neumann boundary condition for the ambient mixture composition, pressure, and temperature. The injector is placed at the center of one of the chamber walls. The mesh configuration used in [25] is employed in the present study which involves an isotropic cell size of 0.5 mm within the spray combustion region. This mesh configuration was shown to reach mesh independence in [25].

4. Model validation

4.1. Inert spray validation

Model evaluation is performed on evaporating sprays (Cases 1–9 shown in Table A1) at different ρ_{am} and D_{noz} values by computing the liquid penetration length (LPL) and vapor penetration length (VPL). This is first carried out by performing inert spray simulations where O_2 is set to zero. LPL is defined as the maximum axial location from the injector to the location where 95% of the total liquid mass is found; VPL is determined using the farthest downstream location of 0.1% fuel mass fraction.

Since experimental data are not available, model evaluation of the liquid-phase is carried out by comparing against the LPL obtained from the liquid scaling law [16]. The liquid properties of *n*-heptadecane are used in the liquid scaling law to produce Diesel #2 liquid length [16] since these resemble the properties of Diesel #2. Fig. 1 shows the computed LPL and VPL for different D_{noz} at different ρ_{am} of 14.8, 30.0,

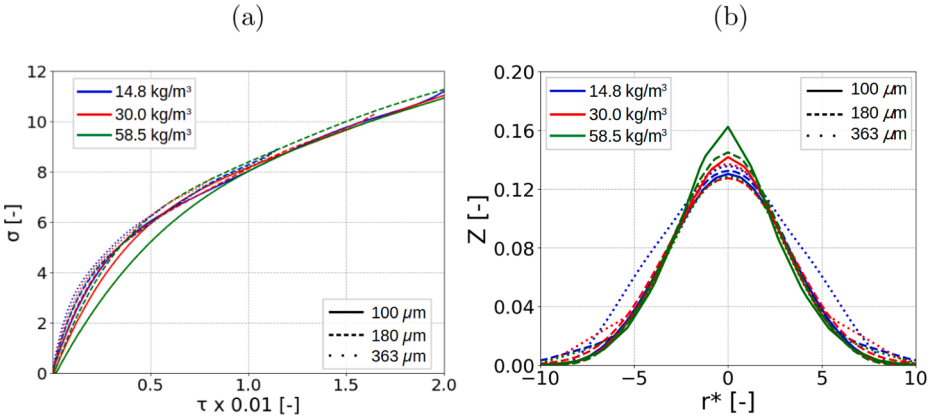

Fig. 2. (a) Dimensionless penetration length (σ) as a function of dimensionless penetration time (τ) and (b) mixture fraction (Z) distribution along normalized radial direction (r^*) at normalized axial distance, $x^* = 40$ for different ρ_{am} of 14.8, 30.0, and 58.5 kg/m^3. Solid-, dashed-, and dotted-lines are results for D_{noz} of 100, 180, and 363 μm, respectively.

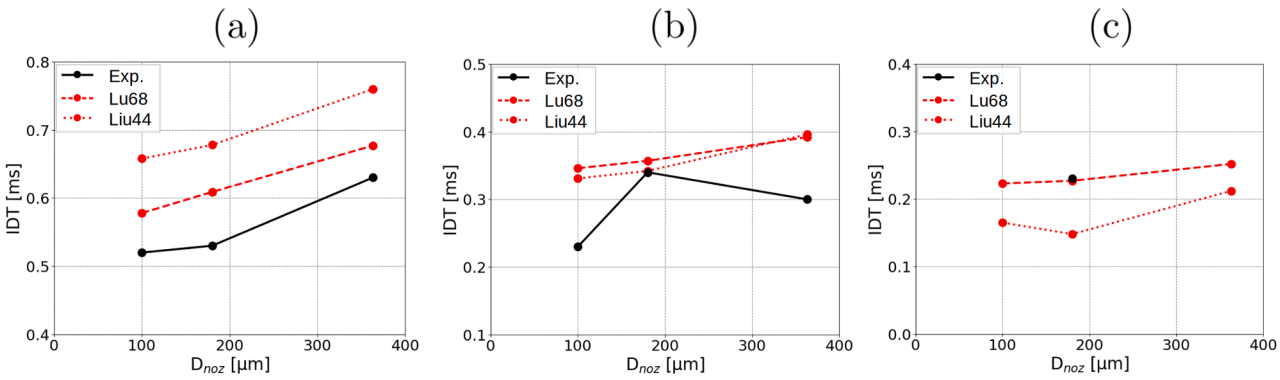

Fig. 3. Ignition delay time (IDT) as a function of nozzle diameter (D_{noz}) at different ρ_{am} of (a) 14.8, (b) 30.0, and (c) 58.5 kg/m^3. Solid-lines denote experimental results. Dashed- and dotted-lines denote the simulation results from Lu68 and Liu44 mechanisms, respectively.

and 58.5 kg/m^3. In the figure, the computed LPL are shown to be comparable to the LPL obtained from the liquid scaling law across different ρ_{am}.

On the other hand, the associated VPLs shown in Fig. 1 are evaluated using the dimensionless penetration length, σ and dimensionless penetration time, τ. Detailed methodology to calculate σ and τ can be found in [17]. As seen in Fig. 2a, all the σ curves collapse on to one another, which agrees with the trend reported in [17]. This indicates that the dependence of VPL on D_{noz} and ρ_{am} is successfully simulated by the model.

It is shown in [10,22] that the profiles of mixture fraction for two different D_{noz} collapse onto one another in normalized coordinates. Therefore, similar methodology from [10,22] is applied to analyze the profiles of mixture fraction for Cases 1–9 (in Table A1. Fig. 2b shows the mixture fraction (Z) fields from cases with varying ρ_{am} and D_{noz} (Cases 1–9) compared together in normalized radial (r^*) and axial (x^*) coordinates. The normalized coordinates r^* and x^* are computed by normalizing the radial (r) and axial coordinate (x) by the equivalent diameter (d_{eq}) of each nozzle, i.e., $r^* = r/d_{eq}$ and $x^* = x/d_{eq}$ [10,22]. The equivalent diameter is calculated as $d_{eq} = D_{noz}\sqrt{\rho_f/\rho_{am}}$, where ρ_f denotes the density of the fuel. It is shown in Fig. 2b that the mixture fraction profiles from different ρ_{am} and D_{noz} collapse onto one another. This implies that the dependence of mixture fraction distribution on ρ_{am} and D_{noz} is also successfully simulated by the model.

4.2. Reacting spray validation

Two *n*-heptane (C_7H_{16}) mechanisms are evaluated in this section. The two mechanisms are the reduced C_7H_{16} mechanism (68 species and 283 reactions) developed by Lu et al. [34], and the mechanism (44 species and 112 reactions) developed by Liu et al. [35]. The mechanisms are henceforth denoted as Lu68 and Liu44, respectively. These two mechanisms have shown good performance in spray combustion context [24,25,32,36]. The IDTs predicted by the two mechanisms for different D_{noz} and ρ_{am} are simulated and compared against the measurement data [1], as shown in Fig. 3. The IDT is defined as the time taken for the mixture temperature to increase by 400 K from its initial temperature ($\Delta T = 400$ K), following the definition in [25]. The IDT predicted by Liu44 overpredicts the IDT by 27% in the low density case (14.8 kg/m^3), but underpredicts by 37% in the high density case (58.5 kg/m^3). Overall, the results from Lu68 are in better agreement than those of Liu44 with the experimental data. For a fixed D_{noz}, the computed IDTs are shown in Fig. 3 to decrease with increasing ρ_{am}, which correspond with measurements. At all three ρ_{am}, the simulated IDTs are shown to increase with D_{noz}. This agrees with the measurement trend at $\rho_{am} = 14.8$ kg/m^3. However, a non-monotonic trend is observed for the measurement data at 30.0 kg/m^3 where the IDT increases from 100 to 180 μm, but decreases from 180 to 363 μm. This discrepancy may be due to the experimental uncertainties caused by the hydraulic delay during fuel injection [37]. Despite this, the relative errors across different ρ_{am} and D_{noz} are less than 50% for the Lu68 mechanism. In addition to this, the performance of the Lu68 mechanism in a zero-dimensional homogeneous reactor is available in the Appendix A1.

5. Results & discussion

In this section, the autoignition characteristics for different D_{noz} at ρ_{am} of 14.8 kg/m^3 (Fig. 4), 30.0 kg/m^3 (Fig. 6), and 58.5 kg/m^3 (Fig. 8) are studied using scatter plots of the temperature-mixture fraction (*T*-*Z*) and contours of various combustion products. For all the cases (shown in Table A1), the low-temperature ignition first initiates in the fuel-lean region ($Z < Z_{st}$), where Z_{st} is the stoichiometric mixture fraction with a value of 0.062. It is followed by a temperature rise within the fuel-rich region ($Z > Z_{st}$). Thereafter, the high-temperature combustion occurs within a relatively less-rich mixture. These observations agree with the findings by Pei et al. [38]. Despite this, there are still distinct differences in the ignition characteristics as ρ_{am} and D_{noz} change, which will be discussed in detail in the following sections.

5.1. Ignition characteristics at $\rho_{am} = 14.8 kg/m^3$

For the 100 μm case at 14.8 kg/m^3, high concentration of RO_2 is shown to form in the fuel-rich inner core of the spray at $t = 0.540$ ms (cf. Fig. 4a). Through the low-temperature reaction pathway, RO_2 oxidizes to form ketohydroperoxide (KET) which also resides in the inner core of the spray. At this time instance, HO_2 radicals form around the vicinity of KET where the spray region is fuel-rich, as shown in Fig. 4a. The *T*-*Z* diagram in Fig. 4a also shows the presence of OH in the fuel-rich side with a peak temperature of ~1100 K. It is notable that RO_2, KET and HO_2 are formed downstream of the liquid fuel.

At $t = 0.588$ ms (Fig. 4b), high concentration of HO_2 is seen forming at two distinct regions in the spray: the L-region which has low local temperature with fuel-richer mixture composition, and the H-region which has relatively higher local temperature as well as less fuel-rich mixture composition. Moreover, it is illustrated in Fig. 4b that OH is present at the H-region, thus implying that HO_2 has been consumed and undergone high-temperature reaction to form OH. The local temperature is also shown to increase beyond the temperature threshold of 1400 K (400 K above T_{am}), which indicates the onset of the main ignition.

The ignition characteristics for the 180 and 363 μm nozzle cases are illustrated in Figs. 4d-f and 4g-i, respectively. During the low-temperature ignition stage at 0.574 ms, HO_2 and OH are present at the fuel-rich side in the 180 μm case (cf. Fig. 4d). It is also important to note that the high-temperature ignition in all three D_{noz} cases occurs in the fuel-rich side at ρ_{am} of 14.8 kg/m^3.

A noticeable difference when D_{noz} increases is the low- and high-

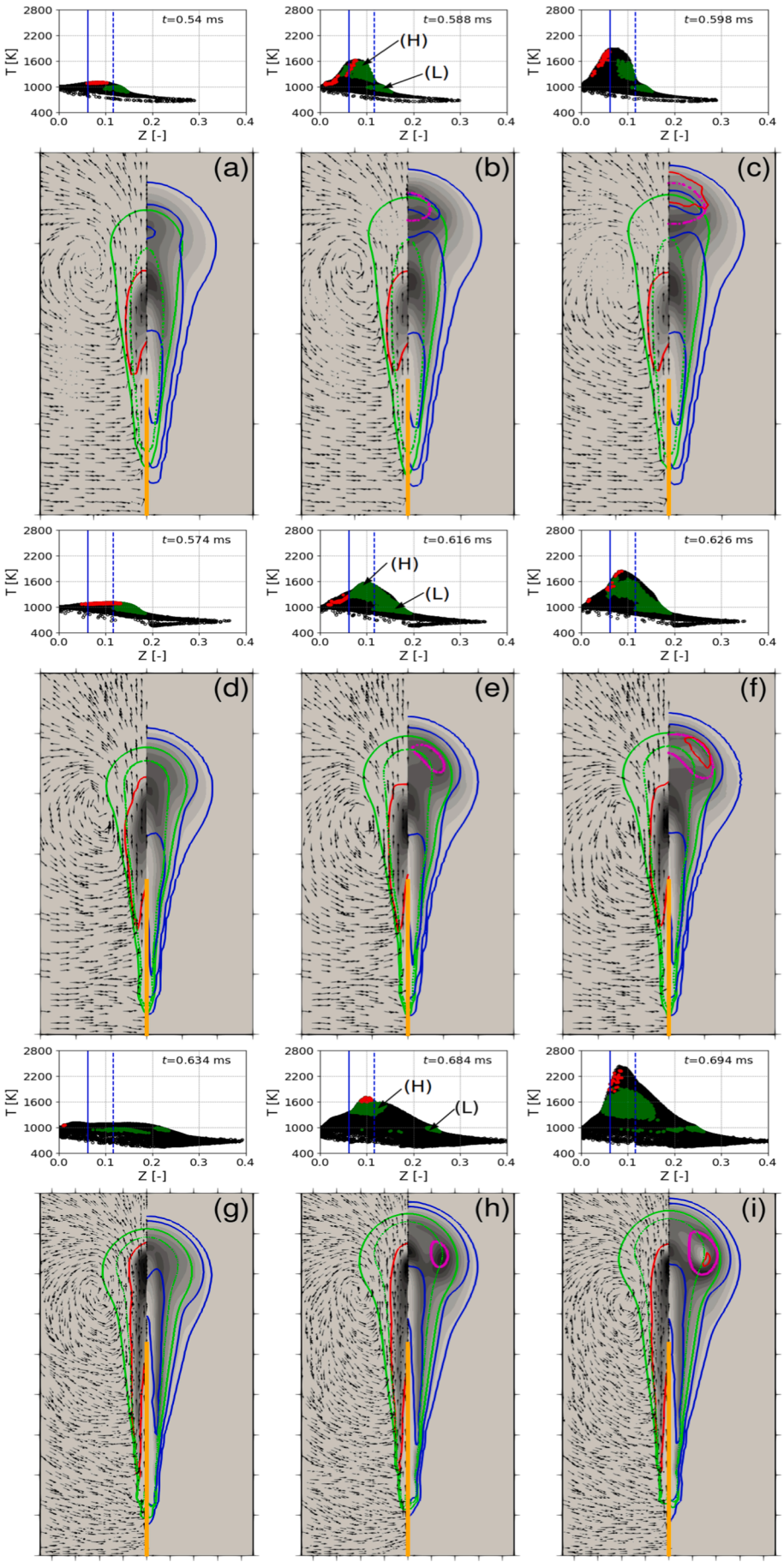

Fig. 4. Velocity vectors and contours of combustion products in the 14.8 kg/m^3 case for D_{noz} of (a–c) 100 µm, (d–f) 180 µm, and (g–i) 363 µm. Above them are their corresponding scatter plot of temperature-mixture fraction (*T*-*Z*). Left, middle and right columns represent the low-temperature ignition stage, onset of high-temperature ignition, and formation of a classical diesel spray flame. Scatter plots: Cells with substantial formation of HO_2 and OH are marked wth green and red, respectively. The thresholds are set to 70% of their respective maximum mass fraction. Stoichiometric and most reactive mixture fractions are represented by solid blue and dashed blue lines, respectively. Contours (a–i): (Left) Ketohyroperoxide contour with velocity vectors (black arrows) and RO_2 mass fraction of 0.001 (solid red); and (Right) HO_2 contour with isolines of scalar dissipation rates of 1, 10, and 100 (solid blue), OH mass fraction of 1×10^{-4} (solid red), and temperature of 1400 K (magenta). Maximum mass fraction of KET and HO_2 are fixed at 0.003 and 0.0006, respectively. Solid green lines indicate the stoichiometric line and the orange line represent the averaged liquid length. Each frame in (a–c) shows 20×40 mm, (d–f) shows 30×60 mm, and (g–i) shows 45×90 mm. (For interpretation of the references to colour in this figure legend, the reader is referred to the web version of this article.)

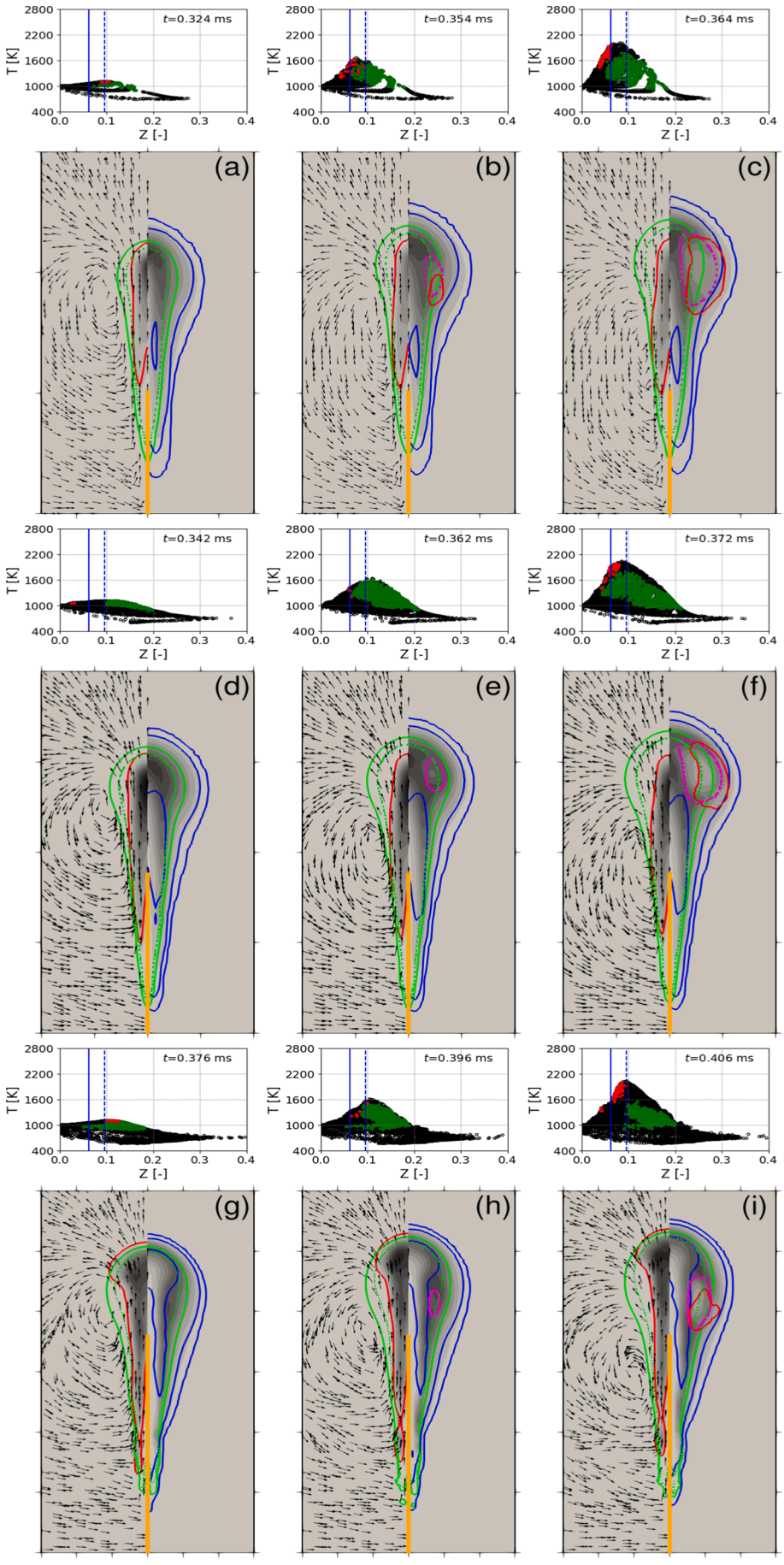

Fig. 6. Velocity vectors and contours of combustion products in the 30.0 kg/m^3 case for D_{noz} of (a–c) 100 µm, (d–f) 180 µm, and (g–i) 363 µm at different times. Above them are their corresponding scatter plot of temperature-mixture fraction (*T*-*Z*). Descriptions can be found in the caption of Fig. 4. Each frame in (a–c) shows 15 × 30 mm, (d–f) shows 20 × 40 mm, and (g–i) shows 30 × 60 mm. (For interpretation of the references to colour in this figure legend, the reader is referred to the web version of this article.)

temperature ignition process occurring later in time. This is expected as the IDT is shown previously to increase with increasing D_{noz} (cf. Fig. 3). The effects of D_{noz} and ρ_{am} on IDT will be further discussed in Section 5.4. Meanwhile, it is shown in Fig. 4 that the onset of high-temperature ignition occurs at the spray head for D_{noz} of 100 μm, which is similarly obtained in the 3-D large eddy simulations by Irannejad et al. [39]. However, the ignition location is seen to shift to the spray periphery as D_{noz} increases to 363 μm. This can be attributed to the overly fuel-rich region in the spray central region as D_{noz} increases. Fig. 5 shows the scatter plots of T, colored by different ranges of Z, along the spray axis for both the central and peripheral region of different D_{noz} at ρ_{am} = 14.8 kg/m^3. The radial distance from the spray axis is denoted as R. The central region of the spray is defined as the region where $R \leqslant d_{eq}$, while the peripheral region is defined as $R > d_{eq}$. The onset of high-temperature ignition is observed at both the spray center and periphery for the 100 μm case, as depicted in Fig. 5a. However, as D_{noz} increases to 180 μm and 363 μm, the onset of high-temperature ignition is shown to occur at the spray periphery (cf. Figs. 5b and c), where the temperature rise in spray central region of the latter case is significantly lower than in the spray periphery.

Moreover, the evaporative cooling of the injected liquid fuel reduces the temperature of the mixtures at the inner spray region near the LPL, as compared to that in the spray periphery (cf. Fig. 5). The overly fuel-rich region ($Z > 0.2$), which has a lower temperature, in the spray central region is, hence, expected to be unfavorable for ignition. This observation is supported by findings from the large eddy simulation results in [23] and the two-dimensional direct numerical simulation conducted by Krisman et al. [40]. It is shown that the cool-flame takes a longer time to reach the most fuel-rich mixture [40]. Meanwhile, the fuel-rich mixture itself takes a longer time to have a spontaneous ignition due to having a longer low-temperature IDT as shown in the zero-dimensional homogeneous reactor simulation results (see Fig. A1 in Appendix A1). This corresponds well to the findings in [41]. These reasons may explain the observation where the high-temperature ignition is more inclined to occur at the spray periphery than at the spray center region as D_{noz} increases.

5.2. Ignition characteristics at ρ_{am} = 30.0 kg/m^3

At a higher ambient density of ρ_{am} = 30.0 kg/m^3 (Fig. 6), the formation of RO_2, KET, and HO_2 starts earlier for the 100 μm nozzle case. From Fig. 6a, HO_2 is also formed in the fuel-rich region where local temperature exceeds 1100 K. The same phenomenon is observed for the larger D_{noz} cases of 180 and 363 μm. However, at this high ρ_{am}, HO_2 does not form at two distinct regions during the onset of high-temperature ignition as that observed at a lower ρ_{am} of 14.8 kg/m^3. Instead, HO_2 is shown to form across a wide range of Z and T, as shown in the T-Z diagrams of Fig. 6b, e, and h. The high-temperature ignitions across different D_{noz} occur at the fuel-rich side. This observation is similar to that observed in the 14.8 kg/m^3 case discussed above, although the transition period from low- to high-temperature ignition is now shorter. This is expected as a shorter transition is also observed in the homogeneous reactor calculation (see Fig. A1 in Appendix A1) as well as in [25]. With a shorter transition time, the ignition location are now nearer to the liquid jet which is highly fuel-rich at the inner core. This, consequently, results in the ignition location to occur at the spray periphery which is relatively less fuel-rich. Fig. 7 shows the scatter plots of T, colored by different ranges of Z, along the spray axis for both the central and peripheral region of different D_{noz} at ρ_{am} of 30.0 kg/m^3. In all three D_{noz} cases, the high-temperature ignitions occur at $R > d_{eq}$ as well as being closer to the liquid jet. As shown in the top row of Fig. 7, the inner cores of the spray are more fuel-rich ($Z > 0.2$) and have low temperature, which makes them unfavorable for ignition to occur. The above explanation agrees with the experimental results presented by Higgins et al. [19] for D_{noz} = 246 μm.

5.3. Ignition characteristics at ρ_{am} = 58.5 kg/m^3

The phenomena are akin to those observed at 30.0 kg/m^3. From Fig. 8, it is also obvious that the ignition locations for all three D_{am} are all at the spray periphery. This can again be explained by analyzing the T and Z along the spray axis. Fig. 9 shows the scatter plots of T, colored by different ranges of Z, along the spray axis for both the central and peripheral region of different D_{noz} at ρ_{am} = 58.5 kg/m^3. From the figure, the inner core is shown to be too fuel-rich to be conducive for ignition, thus ignition occurs at the sides instead. Furthermore, it is also illustrated in Fig. 9 that the ignition location is closer to the liquid jet at this high ρ_{am} condition than in the low ρ_{am} cases. This is expected as the ambient density increases even further, the transition from low- to high-temperature ignition shortens considerably. This consequently leads to the ignition to occur much closer to the liquid jet.

In this high ρ_{am} case of 58.5 kg/m^3, the high-temperature ignitions for both 100 μm and 180 μm cases occur at fuel-lean region. The observation for the 180 μm case agrees with a similar work from the literature [25] which simulated the exact same setup by using a smaller n-heptane mechanism. However, this is not the case when D_{noz} increase to 363 μm which shows the ignition to occur at the fuel-rich region. This difference is likely attributed to the longer IDT for the 363 μm, 58.5 kg/m^3 case, which causes a significant amount of HO_2 to form in the fuel-rich region and consequently resulting in the fuel-rich mixture igniting. Another reason can be related to the overly fuel-rich mixture at the spray core as shown in Fig. 9c. Evaporative cooling is more significant in the large nozzle case as more liquid fuel is injected and longer LPL is observed. The stronger evaporative cooling of the liquid fuel in the large nozzle case prevents ignition to occur at $Z < 0.1$ as observed in the 100 and 180 μm cases (cf. Figs. 9a and 9b). Only until the cool-flame has spread to a relatively fuel-rich region which then leads to a high-temperature ignition. This also resulted in a longer IDT observed for the 363 μm nozzle case.

5.4. Effects of D_{noz} and ρ_{am} on ignition delay time

As shown previously (Fig. 3) the IDT increases as D_{noz} increases. This can be attributed to the different values of local scalar dissipation rate (χ) for different D_{noz} and at varying ρ_{am}, as shown in Fig. 10. Fig. 10 shows the scatter plot of OH and χ for varying D_{noz} at ρ_{am} of (a) 14.8 kg/m^3, (b) 30.0 kg/m^3, and (c) 58.5 kg/m^3 during the onset of high-temperature ignition. From the figure, the χ for the 363 μm nozzle case is consistently larger than the 100 μm case by at least a factor of 3. A high χ leads to longer IDT [41], hence explaining the longer IDT obtained as D_{noz} increases.

It is also depicted in Fig. 3 that IDT becomes shorter as ρ_{am} increases. As aforementioned in Section 5.2, the shorter IDT is likely attributed to the shorter chemical time scale when the ambient density increases. The findings are supported by the homogeneous reactor results (see Fig. A1 in Appendix A1) and the results in [25], which show shorter IDT as ρ_{am} increases from 14.8 to 58.5 kg/m^3.

6. Conclusion

The present work performed an Unsteady Reynolds Averaged Navier-Stokes simulations coupled with Eulerian Stochastic Field method to study the effects of nozzle diameter (D_{noz}) and ambient density (ρ_{am}) on ignition characteristics in Diesel #2 spray flames. The numerical model is able to capture the ignition processes for different D_{noz} of 100, 180, and 363 μm at ρ_{am} of 14.8, 30.0, and 58.5 kg/m^3. Comparisons to measurements show that the ignition delay times are well predicted.

For the low density case (14.8 kg/m^3), the high-temperature ignition location is predicted to shift from the spray tip towards the spray periphery as D_{noz} increases. The current result suggests that the mixture at the spray central region (including the spray tip) are getting more fuel-

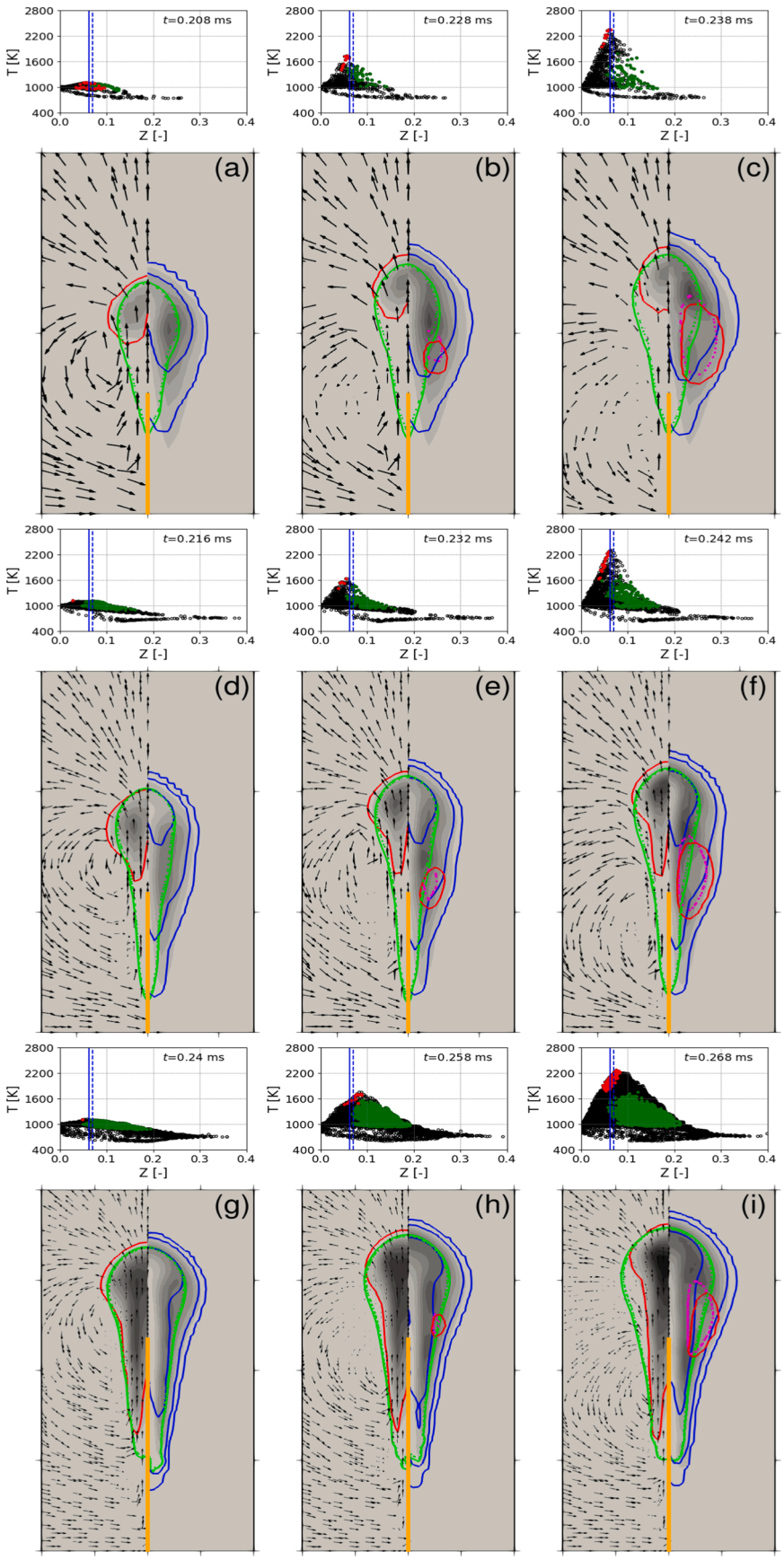

Fig. 8. Velocity vectors and contours of combustion products in the 58.5 kg/m^3 case for D_{noz} of (a–c) 100 µm, (d–f) 180 µm, and (g–i) 363 µm at different times. Above them are their corresponding scatter plot of temperature-mixture fraction (*T*-*Z*). Descriptions can be found in the caption of Fig. 4. Each frame in (a–c) shows 10 × 20 mm, (d–f) shows 15 × 30 mm, and (g–i) shows 20 × 40 mm.

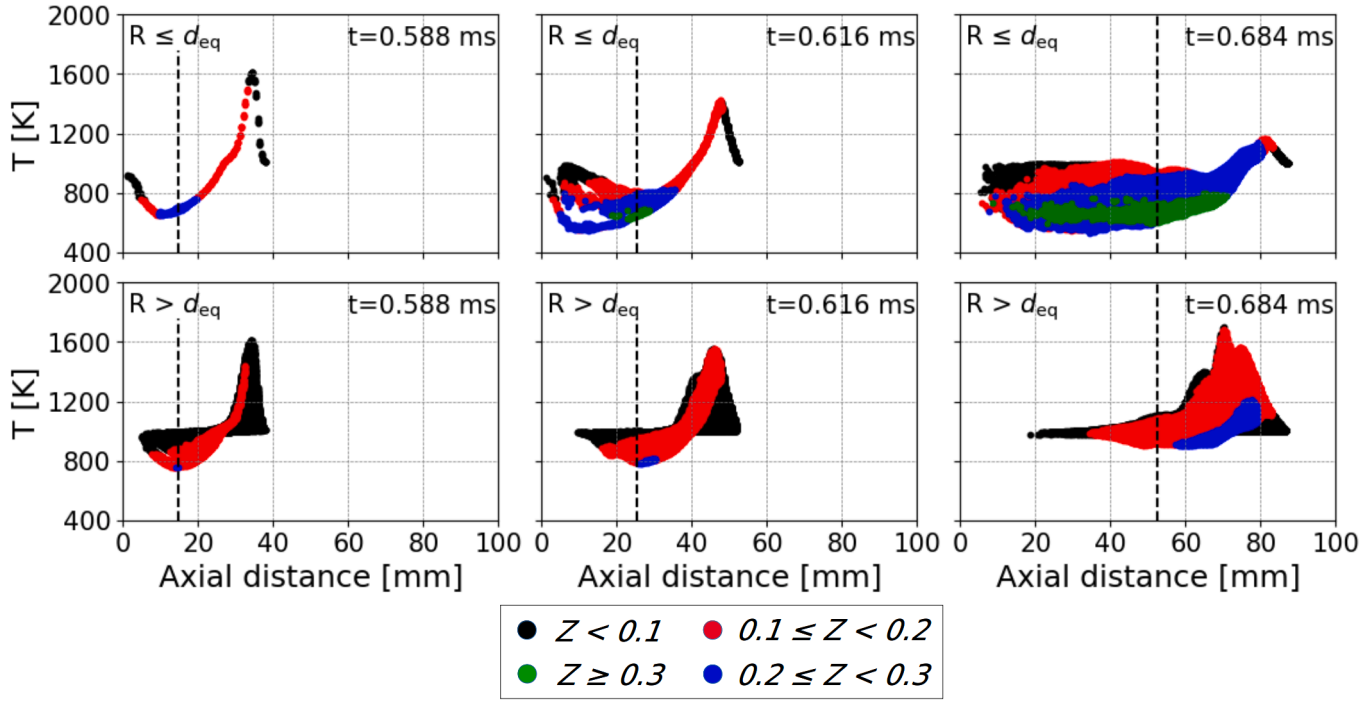

Fig. 5. Scatter plots of temperature (T) colored by different ranges of mixture fraction (Z) at the onset of high-temperature ignition for D_{noz} of (a) 100 μm, (b) 180 μm, and (c) 363 μm at ρ_{am} of 14.8 kg/m^3. Dashed vertical lines represent the liquid penetration length. Top row: spray central region ($R \leqslant d_{eq}$). Bottom row: spray periphery ($R > d_{eq}$).

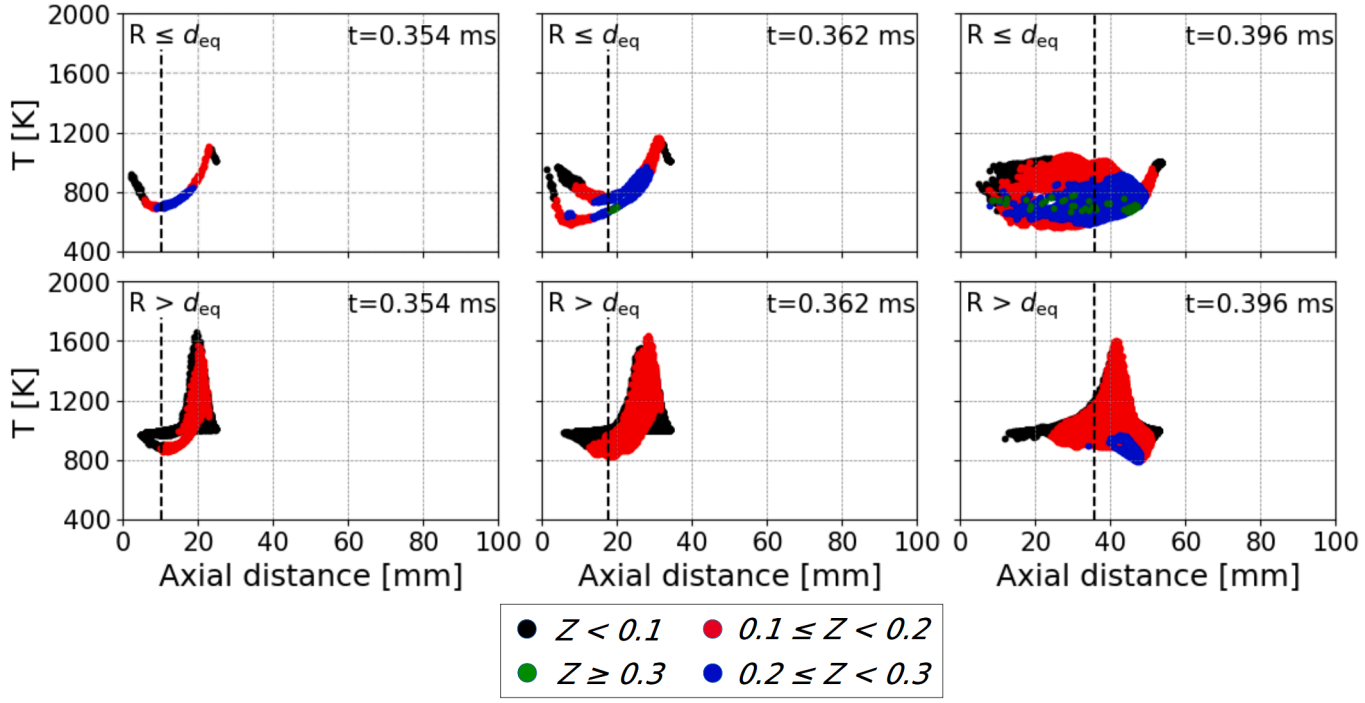

Fig. 7. Scatter plots of temperature (T) colored by different ranges of mixture fraction (Z) at the onset of high-temperature ignition for D_{noz} of (a) 100 μm, (b) 180 μm, and (c) 363 μm at ρ_{am} of 30.0 kg/m^3. Dashed vertical lines represent the liquid penetration length. Top row: spray central region ($R \leqslant d_{eq}$). Bottom row: spray periphery ($R > d_{eq}$). (For interpretation of the references to colour in this figure legend, the reader is referred to the web version of this article.)

rich ($Z > 0.2$) as D_{noz} increases. This leads to the spray central region being unfavorable for ignition due to being overly fuel-rich and having lower temperature. Instead, the ignition occurs at the periphery of the spray where $Z \lesssim 0.2$. As ρ_{am} increases to 30.0 and 58.5 kg/m^3, the ignition locations for all D_{noz} cases are occurring at the spray periphery. This is because of the shorter ignition timing and the overly fuel-rich spray central region.

The numerical results show that the mixture fraction of the first igniting mixture during the high-temperature ignition across different D_{noz} are at the fuel-rich region at ρ_{am} of 14.8 and 30.0 kg/m^3. However,

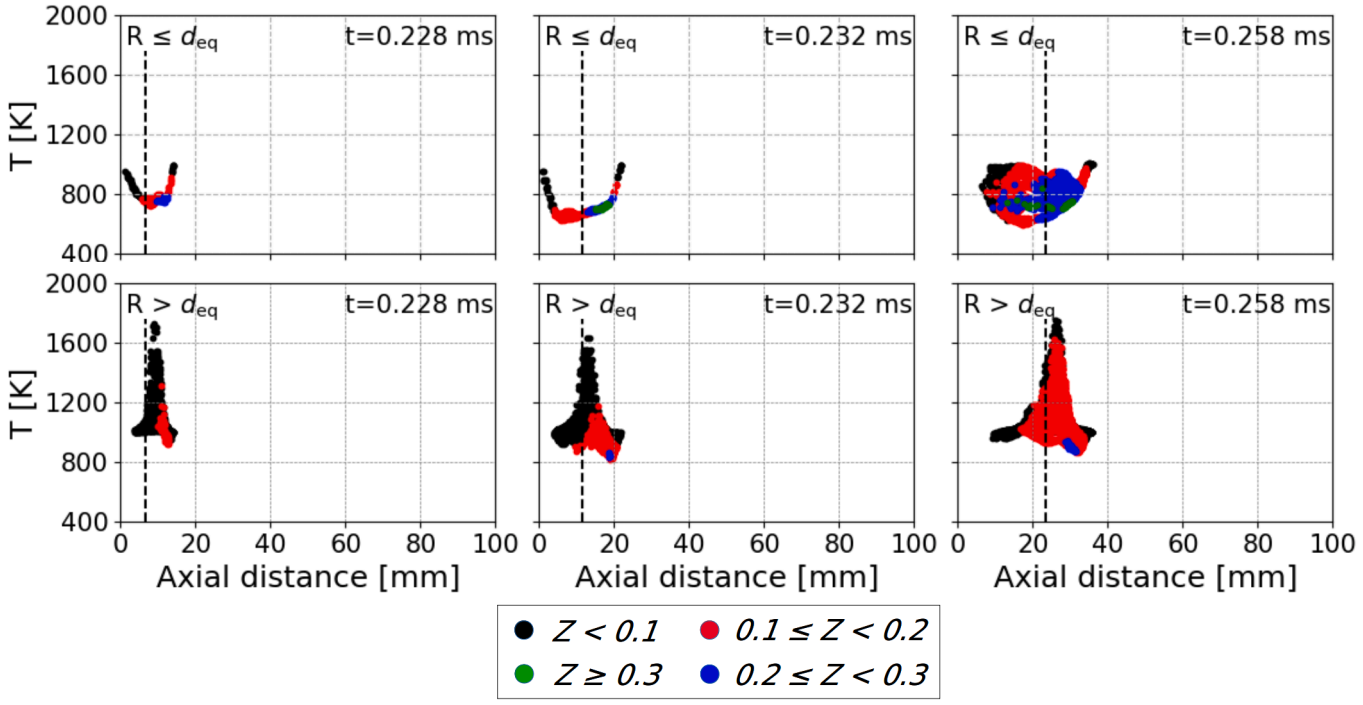

Fig. 9. Scatter plots of temperature (T) colored by different ranges of mixture fraction (Z) at the onset of high-temperature ignition for D_{noz} of (a) 100 µm, (b) 180 µm, and (c) 363 µm at ρ_{am} of 58.5 kg/m^3. Dashed vertical lines represent the liquid penetration length. Top row: spray central region ($R \leq d_{eq}$). Bottom row: spray periphery ($R > d_{eq}$).

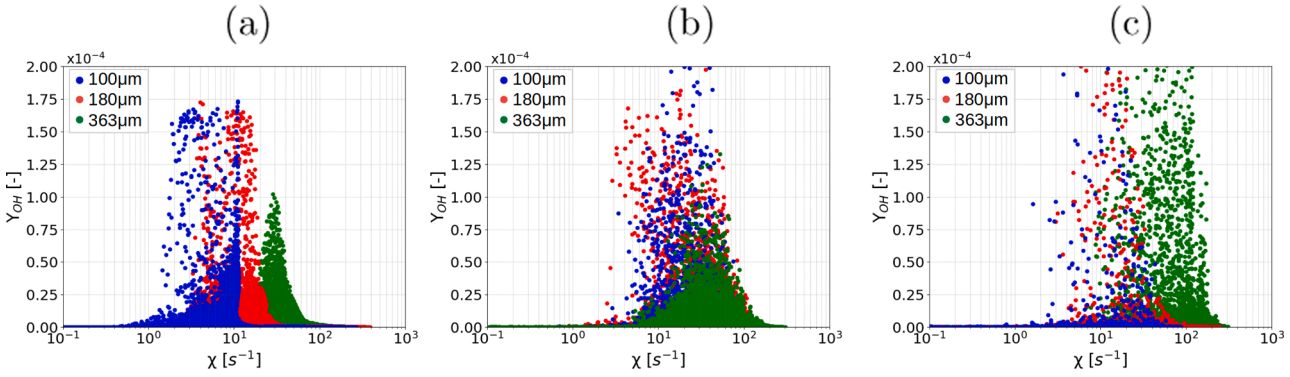

Fig. 10. Scatter plots of mass fraction of OH and scalar dissipation rate (OH-χ) at the onset of high-temperature ignition for different ρ_{am} of (a) 14.8 kg/m^3, (b) 30.0 kg/m^3, and (c) 58.5 kg/m^3, as well as D_{noz} of 100, 180, and 363 µm.

this is not the case when ρ_{am} increases to 58.5 kg/m^3. The igniting mixture still occurs at the fuel-rich region for the 363 µm nozzle case, but it occurs at the fuel-lean side for the D_{noz} cases of 100 and 180 µm. This can be attributed to the relatively longer ignition delay time in the 363 µm nozzle case. The longer ignition delay time as D_{noz} increases can be related to the higher local scalar dissipation rate observed in the large nozzle case.

CRediT authorship contribution statement

Jiun Cai Ong: Conceptualization, Investigation, Validation, Writing - original draft. **Jens Honore Walther:** Conceptualization, Supervision, Writing - review & editing, Supervision, Funding acquisition. **Shijie Xu:** Software, Validation, Writing - review & editing. **Shenghui Zhong:** Software, Validation, Writing - review & editing. **Xue-Song Bai:** Conceptualization, Software, Writing - review & editing. **Kar Mun Pang:** Conceptualization, Validation, Supervision, Writing - review & editing.

Declaration of Competing Interest

The authors declare that they have no known competing financial interests or personal relationships that could have appeared to influence the work reported in this paper.

Acknowledgements

The authors gratefully acknowledge the financial support from the Independent Research Fund Denmark (DFF), MAN Energy Solutions under the Grant No. 8022-00143B, and the Swedish Research Council (VR). The computation was performed using Niflheim cluster at Technical University of Denmark (DTU).

Appendix A

A.1. Autoignition in 0-D homogeneous reactor

The autoignition characteristics of Lu68 mechanism is first evaluated by performing a zero-dimensional (0-D) homogeneous reactor calculations at three different initial ambient density (ρ_{am}) of 14.8, 30.0, and 58.5 kg/m^3 and three different nozzle diameter (D_{noz}) of 100, 180, and 363 μm using the Ansys CHEMKIN-PRO software. The high-temperature ignition delay time (IDT_{HT}) here is defined as the time where the mixture temperature increase to 400 K above the initial temperature ($T_{t=0}$). Mass fraction of heptyl radical, $C_7H_{15}O_2$ (RO_2 is henceforth used for brevity) is used as an indicator for the low-temperature ignition (LTI) activity. Therefore, the low-temperature ignition delay time (IDT_{LT}) is defined here as the time where the maximum mass fraction of RO_2 is attained.

A quadratic correlation (Eq. (1)) between temperature and mixture fraction can be obtained by postprocessing the 3D-CFD reacting case results prior to the onset of LTI.

$$T_{t=0} = T_{am} + 1120Z^2 - 1370Z \quad (1)$$

In Eq. (1), Z denotes the mixture fraction while T_{am} denotes the initial ambient temperature in the combustion chamber which is set as 1000 K. This quadratic correlation corresponds to the mixing of vapor fuel and hot ambient air. Therefore, it is also known as the spray mixing line. Eq. (1) is constructed for $0 \leqslant Z \leqslant 0.4$ and the equation is found to be applicable for all three ρ_{am} and three D_{noz} cases (not shown). The most reactive mixture fraction (Z_{mr}) is defined as the mixture which has the shortest IDT_{HT}, and the associated IDT is known as most reactive IDT (IDT_{mr}).

From Fig. A1a, Z_{mr} is shown to decrease and move towards the stoichiometric mixture fraction (Z_{st}) with increasing ρ_{am}. The Z_{mr} are recorded to be 0.117, 0.096, and 0.070 for the 14.8, 30.0, and 58.5 kg/m^3 cases, respectively. The corresponding $T_{t=0}$ are 855, 879, 905 K. As the same correlation (Eq. (1)) is applicable across different D_{noz} for a given ρ_{am}, the Z_{mr} obtained from Fig. A1a is applicable for all three D_{noz}. This also implies that D_{noz} has no significant effect on Z_{mr} in the present study. In addition to this, Fig. A1a also shows that both IDT_{LT} and IDT_{HT} become shorter as ρ_{am} increases. Furthermore, longer IDTs are obtained as the mixture becomes richer (Z increases) and has a lower temperature ($T_{t=0}$ decreases). It is also worth mentioning that the dwell period between LTI and high-temperature ignition (HTI) decreases as the mixture becomes richer (cf. Fig. A1a). This is similarly shown for *n*-dodecane fuel in [41].

Fig. A1b depicts the simulated heat releases rate (HRR) at the most reactive states for each ρ_{am} case. The temporal evolution of RO_2 of these cases are also provided in the figure. It is evidently shown in Fig. A1b that the LTI and HTI stages coincide with the peak of RO_2 and HRR. Moreover, the HTI stage is also shown to occur after RO_2 is consumed.

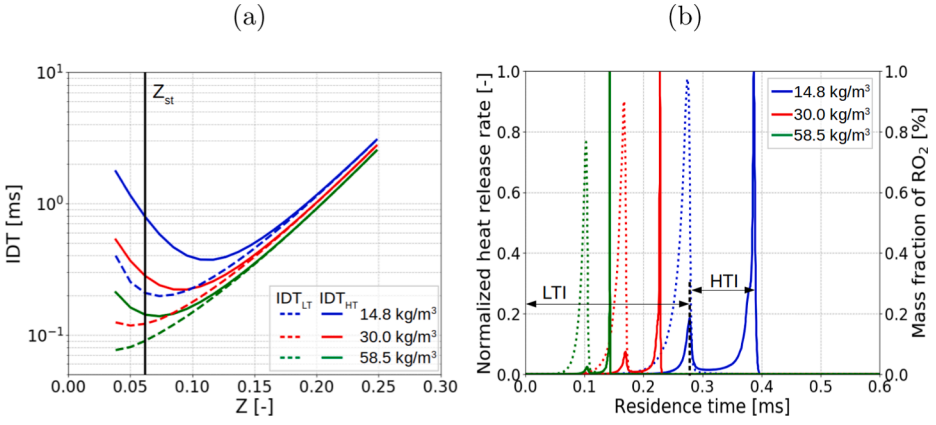

Fig. A1. (a) Low-temperature (IDT_{LT}) and high-temperature ignition delay times (IDT_{LT}) of homogeneous mixtures for various initial mixture fractions (Z) and temperatures (T) at ρ_{am} of 14.8, 30.0, and 58.5 kg/m^3. Solid vertical black line represents stoichiometric mixture fraction (Z_{st}) of 0.062. (b) Temporal evolution of normalized heat release rate (HRR) of Z_{mr} computed in the 0-D homogeneous reactor model at ρ_{am} of 14.8, 30.0, and 58.5 kg/m^3. Solid lines represent the normalized HRR. Dotted lines represent mass fraction of RO_2.

References

[1] Engine combustion network. https://ecn.sandia.gov/.
[2] Pickett LM, Siebers DL. Soot in diesel fuel jets: effects of ambient temperature, ambient density, and injection pressure. Combust Flame 2004;138(1–2):114–35.
[3] Pickett LM, Siebers DL. Orifice diameter effects on diesel fuel jet flame structure. J Eng Gas Turbines Power 2005;127(1):187–96.
[4] Pickett LM, Siebers DL. Soot formation in diesel fuel jets near the lift-off length. Int J Engine Res 2006;7(2):103–30.
[5] Krisman A, Hawkes ER, Talei M, Bhagatwala A, Chen JH. A direct numerical simulation of cool-flame affected autoignition in diesel engine-relevant conditions. Proc Combust Inst 2017;36(3):3567–75.
[6] Dahms RN, Paczko GA, Skeen SA, Pickett LM. Understanding the ignition mechanism of high-pressure spray flames. Proc Combust Inst 2017;36(2):2615–23.
[7] Kundu P, Ameen MM, Som S. Importance of turbulence-chemistry interactions at low temperature engine conditions. Combust Flame 2017;183:283–98.
[8] Pei Y, Hawkes ER, Bolla M, Kook S, Goldin GM, Yang Y, Pope SB, Som S. An analysis of the structure of an n-dodecane spray flame using TPDF modelling. Combust Flame 2016;168:420–35.
[9] Westlye F. PhD Dissertation. Experimental Study of Liquid Fuel Spray Combustion. Technical University of Denmark (DTU); 2016.
[10] Pastor JV, Garcia-Oliver JM, Garcia A, López AM. An experimental investigation on spray mixing and combustion characteristics for spray C/D nozzles in a constant pressure vessel. SAE Technical Paper 2018-01-1783, 2018.
[11] Kyriakides N, Chryssakis C, Kaiktsis L. Influence of heavy fuel properties on spray atomization for marine diesel engine applications. SAE Technical Paper 2009-01-1858, 2009.
[12] Kilpinen P. Optimization of a simplified sub-model for NO emission prediction by CFD in large 4-stroke marine diesel engines. Fuel Process Technol 2010;91(2):218–28.
[13] Ishibashi R, Tsuru D. An optical investigation of combustion process of a direct high-pressure injection of natural gas. J Mar Sci Technol 2017;22(3):447–58.
[14] Schmid A, von Rotz B, Bombach R, Weisser G, Herrmann K, Boulouchos K. Ignition behaviour of marine diesel sprays. In: COMODIA Conference, Fukuoka, Japan, 2012.
[15] Bolla M, Srna A, Wright YM, Von Rotz B, Herrmann K, Boulouchos K. Influence of injector diameter (0.2-1.2 mm range) on diesel spray combustion: measurements and CFD simulations. SAE Technical Paper 2014-01-1419, 2014.
[16] Siebers D. Scaling liquid-phase fuel penetration in diesel sprays based on mixing-limited vaporization. SAE Trans 1999:703–28.
[17] Naber J, Siebers D. Effects of gas density and vaporization on penetration and dispersion of diesel sprays. SAE Trans 1996:82–111.
[18] Siebers D, Higgins B. Flame lift-off on direct-injection diesel sprays under quiescent conditions. SAE Trans 2001:400–21. 2001-01-0530.
[19] Higgins B, Siebers D, Aradi A. Diesel-spray ignition and premixed-burn behavior. SAE Trans 2000:961–84. 2000-01-0940.

[20] Cung K, Bitsis DC, Briggs T, Kalaskar V, Abidin Z, Shah B, Miwa J. Effect of micro-hole nozzle on diesel spray and combustion. SAE Technical Paper, 2018-01-0301, 2018.
[21] Senecal P, Pomraning E, Richards K, Briggs T, Choi C, McDavid R, Patterson M. Multi-dimensional modeling of direct-injection diesel spray liquid length and flame lift-off length using CFD and parallel detailed chemistry. SAE Trans 2003:1331–51.
[22] Desantes JM, García-Oliver JM, Novella R, Pachano L. A numerical study of the effect of nozzle diameter on diesel combustion ignition and flame stabilization. Int J Engine Res.
[23] Ong JC, Pang KM, Bai X-S, Walther JH. Large-eddy simulation of n-dodecane spray flame: effects of nozzle diameter on autoignition at varying ambient temperatures. Proc Combust Inst; 2020 [Article in press].
[24] Pang KM, Jangi M, Bai X-S, Schramm J, Walther JH. Effects of nozzle diameter on diesel spray flames: a numerical study using an eulerian stochastic field method. Energy Proc 2017;142:1028–33.
[25] Pang KM, Jangi M, Bai X-S, Schramm J, Walther JH, Glarborg P. Effects of ambient pressure on ignition and flame characteristics in diesel spray combustion. Fuel 2019;237:676–85.
[26] Pang KM, Jangi M, Bai X-S, Schramm J. Evaluation and optimisation of phenomenological multi-step soot model for spray combustion under diesel engine-like operating conditions. Combust Theory Model 2015;19(3):279–308.
[27] Shih T-H, Liou WW, Shabbir A, Yang Z, Zhu J. A new k-epsilon eddy viscosity model for high reynolds number turbulent flows. Comput Fluids 1995;24(3):227–38.
[28] Reitz RD, Diwakar R. Structure of high-pressure fuel sprays. SAE Trans 1987;870598:492–509.
[29] Lin R, Tavlarides LL. Thermophysical properties needed for the development of the supercritical diesel combustion technology: evaluation of diesel fuel surrogate models. J Supercrit Fluids 2012;71:136–46.
[30] Valino L. A field Monte Carlo formulation for calculating the probability density function of a single scalar in a turbulent flow. Flow Turbul Combust 1998;60(2):157–72.
[31] Jangi M, Lucchini T, Gong C, Bai X-S. Effects of fuel cetane number on the structure of diesel spray combustion: an accelerated Eulerian stochastic fields method. Combust Theory Model 2015;19(5):549–67.
[32] Pang KM, Jangi M, Bai X-S, Schramm J, Walther JH. Modelling of diesel spray flames under engine-like conditions using an accelerated eulerian stochastic field method. Combust Flame 2018;193:363–83.
[33] Jangi M, Yu R, Bai X-S. Development of chemistry coordinate mapping approach for turbulent partially premixed combustion. Flow Turbul Combust 2013;90(2):285–99.
[34] Lu T, Law CK. Strategies for mechanism reduction for large hydrocarbons: n-heptane. Combust Flame 2008;154(1–2):153–63.
[35] Liu S, Hewson JC, Chen JH, Pitsch H. Effects of strain rate on high-pressure nonpremixed n-heptane autoignition in counterflow. Combust Flame 2004;137(3):320–39.
[36] Som S, Senecal PK, Pomraning E. Comparison of RANS and LES turbulence models against constant volume diesel experiments. In: ILASS Americas, 24th Annual Conference on Liquid Atomization and Spray Systems, San Antonio, TX; 2012.
[37] Manin J, Bardi M, Pickett L, Payri R. Boundary condition and fuel composition effects on injection processes of high-pressure sprays at the microscopic level. Int J Multiphase Flow 2016;83:267–78.
[38] Pei Y, Som S, Pomraning E, Senecal PK, Skeen SA, Manin J, Pickett LM. Large eddy simulation of a reacting spray flame with multiple realizations under compression ignition engine conditions. Combust Flame 2015;162(12):4442–55.
[39] Irannejad A, Banaeizadeh A, Jaberi F. Large eddy simulation of turbulent spray combustion. Combust Flame 2015;162(2):431–50.
[40] Krisman A, Hawkes ER, Chen JH. A parametric study of ignition dynamics at ECN Spray A thermochemical conditions using 2D DNS. Proc Combust Inst 2019;37(4):4787–95.
[41] Borghesi G, Krisman A, Lu T, Chen JH. Direct numerical simulation of a temporally evolving air/n-dodecane jet at low-temperature diesel-relevant conditions. Combust Flame 2018;195:183–202.